ELSEVIER

PII: S0011-2275(98)00049-6

Cryogenics **38** (1998) 743–756

Printed in Great Britain
0011-2275/98/$—see front matter

'Electromaglev' ('active-maglev')—magnetic levitation of a superconducting disk with a DC field generated by electromagnets: Part 3. Theoretical results on levitation height and stability

Makoto Tsuda, Haigun Lee and Yikikazu Iwasa*

Francis Bitter Magnet Laboratory, Massachusetts Institute of Technology, Cambridge, MA 02139, USA

Received 3 March 1998

We present Part 3 results of a comprehensive theoretical study of an 'electromaglev' ('active-maglev') system, in which a high-temperature superconducting bulk YBCO sample is levitated stably in a DC magnetic field generated by a magnet system. Field solutions have been obtained numerically to compute levitation height and define stability criteria for the superconducting disk sample. Our analysis assumes that the disk, which otherwise obeys the Bean critical-state model, traps flux when cooled in the presence of a field from the normal state to the superconducting state. Indeed it is shown that the trapped flux makes subtle and crucial changes in field distribution (and thus current density distribution) in the disk, which differ from those in a disk strictly obeying the Bean model used in the zeroth-order theory. The analysis confirms a key experimental finding that the trapped flux is another essential element for determining levitation height and ensuring tilt-free stable levitation. For stability, trapped flux is in addition to at least two degrees of freedom for spatial supercurrent flow and the profile conditions imposed on the field generated by the magnet system. Procedures to produce stable, tilt-free levitation are described. Agreement between experiment and analysis on dependence of levitation height on magnet current is quite good. The analysis also shows that to achieve stable levitation, a YBCO ring sample requires a radial build that is sufficiently thick to permit the supercurrent to flow in the radial direction. The minimum radial build required, ΔR_{min}, for a YBCO ring of outside radius 12.5 mm operating at 77 K is typically ~ 50 μm. An analytical expression that gives approximate values of ΔR_{min} has also been derived; ΔR_{min} depends inversely on the square of the critical current density of the superconductor.

Keywords: F. magnetic levitation; active maglev; YBCO disk; magnetic field analysis; Bean's critical-state model

We have been studying an 'electromaglev' ('active-maglev') system, in which a superconducting bulk sample is levitated stably in a DC magnetic field[1-3]. *Figure 1* shows a cross-sectional drawing of an active-maglev system used to generate both experimental and analytical results reported here. The system consists of: (1) YBCO float (disk in this figure); (2) electromagnets (inside and outside coils); and steel plates. The entire components are operated immersed in a bath of liquid nitrogen. The focus of the study has been on levitation stability, lift-to-weight ratio, and lateral stiffness. Four YBCO bulk samples have been studied: (1) disk; (2) annulus; (3) the same annulus with a permanent magnet disk placed in the hole; and (4) ring[1-3]; the difference between annulus and ring is explained later. The zeroth-order theory has been developed to interpret the experimental results. Agreement between experiment and theory (zeroth order) on lift-to-weight ratio and lateral stiffness has been excellent, and it validates the basic premise of the zeroth-order theory that lift is the Lor-

*To whom correspondence should be addressed. During the period June 1, 1997 through November 30, 1997 at Department of Electrical Engineering, Keio University, Yokohama, Japan

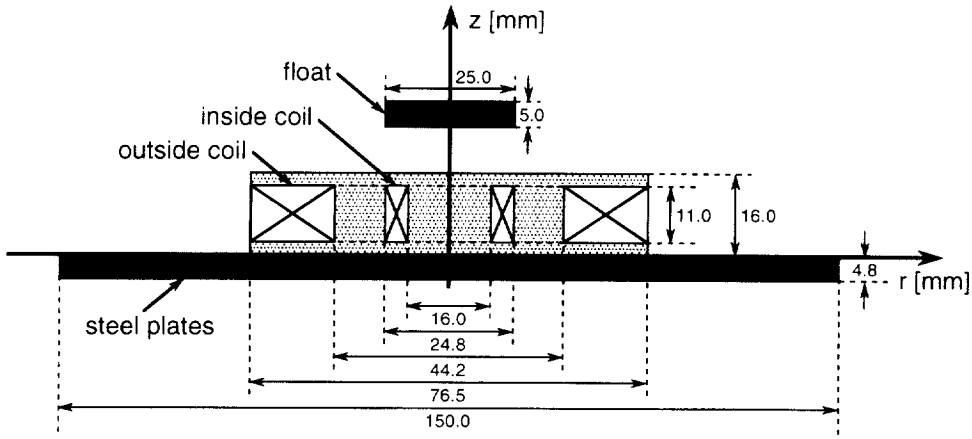

Figure 1 Cross-sectional drawing of an active-maglev system used to generate both experimental and analytical results reported here. The system consists of: (1) YBCO float (disk in this figure); (2) electromagnets (inside and outside coils); and steel plates. The entire components are operated immersed in a bath of liquid nitrogen

entz interaction force between the supercurrent circulating in each YBCO float at the *rim* and the radial component of the magnetic field generated by the magnet system.

This paper presents numerical analyses that lead to field solutions for a YBCO disk exposed to a nonuniform field generated by the magnet system. The field solutions are used to compute levitation height, lift, and moment for the disk. It also presents results of an analysis on two necessary conditions required for a sample to achieve stable levitation: (1) a sufficient level of trapped flux; and (2) at least two degrees of freedom for spatial supercurrent flow. Neither has been included in the zeroth-order theory used in our previous analysis. Discussed in detail are field and critical current density distributions of a disk sample with trapped flux vis-à-vis the stability of the disk, both lateral and pitch.

In the first papers on this work[1,2], we reported unstable levitation observed in the experiment with a pancake coil wound with silver-sheathed BSCCO-2223 tape, and attributed the instability to an induced supercurrent that in the pancake coil would be restricted to flow only in the azimuthal direction as the Amperian current flowing in a permanent magnet disk. An implication is that even a YBCO ring would be unstable if its radial build is too thin; conversely if a silver-sheathed BSCCO-2223 tape has a superconducting layer that is sufficiently thick, a one-turn coil wound with such a tape would be stable. As will be presented here we have discovered that this two-dimensionality of supercurrent distribution is a natural consequence of the magnetic flux distribution within a disk or ring that levitates stably. The analysis uses a disk as the sample configuration; some of the results are then applied to a ring.

Formulation

Equivalent current method

In the zeroth-order theory, the magnetic system consisting of the electromagnets with the steel plates placed underneath is modelled as a steel-less system, in which the steel plates are replaced with another set of electromagnets that is identical to and placed coaxially at an appropriate distance below the original set. This model generates magnetic field values that agree well in the axial component, B_z, but not so well in the radial component, B_r. In this study we have relied on a numerical method, specifically an equivalent current method (ECM)[4–6], to generate accurate field values for the magnetic system. ECM is simpler to execute than more conventional methods such as the finite element method (FEM) and boundary element method (BEM). Appendix A discusses the ECM in more detail.

Bean's critical-state model

The Bean critical-state model may be used to determine the supercurrent distribution in a disk. In the zeroth-order theory, the disk is modelled as a thin slice within a long cylinder of the same radius. Accordingly, an external magnetic field, H_z, directed parallel to the axis of the cylinder penetrates into the disk from its rim, inducing a supercurrent within a thin layer called the penetration depth, which in this model is given by H_z/J_c. In reality, the field of the magnet system is nonuniform and it induces supercurrents at the three surfaces of the disk, top, bottom, and rim. Because H_r that parallels the top and bottom surfaces is much smaller than H_z that parallels the rim, the penetration depth of the supercurrent from the top or bottom surface is much smaller than that from the rim. Among the supercurrents induced in the disk, that looping around the rim thus contributes most to the lift. This conclusion agrees with experimental results[3] that show virtually identical lift forces for three circular samples—disk, annulus, and ring—of the same outside diameters but with presumably different supercurrents at the top and bottom surfaces.

Finite element method (FEM)

As qualitatively described above, field profiles both inside and outside of a thin disk are quite different—particularly the B_r component—from those of a thin slice within a long cylinder. The penetration depth of the disk, also an important parameter for lift, is greater than that of the thin slice. A two-dimensional finite element method (FEM) based on the current vector potential (**T**) method[7,8] was performed to evaluate the supercurrents of the disk at three surfaces. According to the experimental results that show critical current density, J_c, parallel to the a–b plane is ~ 3 times greater than that of the c-axis[9], we may neglect the current flow across the a–b planes and subdivide the disk axially into several thin wafers.

The governing equation in two dimensions, with the

assumption of zero current flow in the axial direction, is given by:

$$\mathbf{n}\cdot\nabla\times\frac{1}{\sigma_s}\nabla\times(T_n\mathbf{n})+\mu_0\frac{\partial T_n}{\partial t}+\frac{\mu_0}{4\pi}\mathbf{n}\cdot\int\frac{\partial T_n}{\partial t}\nabla\left(\frac{1}{r}\right)dS \quad (1)$$

$$=-\mathbf{n}\cdot\frac{\partial\mathbf{B}_n}{\partial t}$$

where $\mathbf{n}$ is the directional vector normal to the surface; σ_s is, as discussed below, an 'appropriate' conductivity of the superconductor; T_n is the current vector potential in the n-direction; r is the distance between source and point of computation; and $\mathbf{B}_n$ is the ambient field generated by the magnet system.

Equation (1), derived in Appendix B, is solved numerically with FEM using the Galerkin method. For applying this conventional eddy current approach to shielding supercurrent analysis, the following constituent equations are used[7]:

$$\mathbf{J}=\sigma_s\mathbf{E};\ \sigma_s=\frac{J_c}{|\mathbf{E}|}\ (\mathbf{E}\neq 0) \quad (2)$$

$$\frac{\partial\mathbf{J}}{\partial t}=0\ (\mathbf{E}=0) \quad (3)$$

The numerical scheme based on the Bean critical state model follows an iterative process in which the conductivity of each element is adjusted to make the amplitude of the current density in that element equal to J_c.

In the numerical analysis, a disk, of radius R_d = 12.5 mm and thickness δ_d = 5 mm, is divided axially into five thin wafers, each 1 mm thick. Each wafer is further divided radially into 49 rings and one disk at the center, each having 0.25 mm radial build. The external field used in the analysis is nonuniform, as generated by the magnet system in the experiment[1-3]. *Figure 2* shows the current density distributions across the disk resting atop the magnet system at a current of 20 A (same amplitude but reverse polarities through the outside and inside coils[3]). The solid and dashed traces correspond, respectively, to those of the first (bottom) and fifth (top) wafers and the dotted trace corresponds to that of the third (middle) wafer. The induced supercurrent in each wafer flows mainly at the rim and its peak value is set at 10^8 A/m^2. The radial penetration depths of the top and bottom wafers are greater than that of the center. This difference in penetration depth is due to the supercurrent near each of the disk surfaces keeping the inside field constant. *Figure 2* also shows the presence of a small amount of current in the region outside the penetration depth. Magnetic flux densities within and in the vicinity of the disk due to the magnet system (at 20 A) and the supercurrent of the disk (within the penetration depth) are calculated with another code based on the Biot–Savart law[10]. *Figure 3* presents three graphs of magnetic vectors, where in each graph the right-hand half of the disk is outlined as a rectangle ($0 \le r \le 12.5$ mm and $0 \le z \le 5$ mm): in *Figure 3*(a) are the magnetic vectors due to the magnet system alone; in *Figure 3*(b) are the magnetic vectors of *Figure 3*(a) plus those due to the supercurrent within the penetration depth; and in *Figure 3*(c) are the magnetic vectors of *Figure 3*(b) plus those due to the supercurrents within the penetration depths at both top and bottom surfaces. Also indicated in each graph is the dotted line tracing the boundary of a long cylinder of radius R_d.

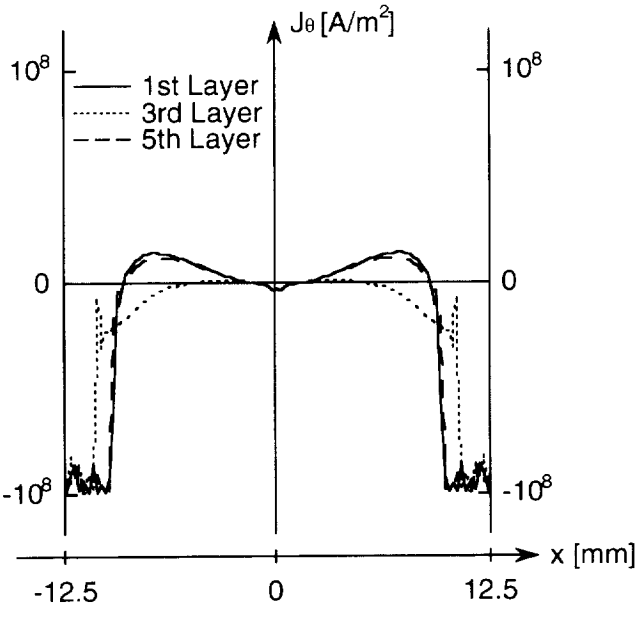

Figure 2 Current density distributions across the disk of radius 12.5 mm and thickness 5 mm as it rests on the the magnet system at a magnet current of 20 A (same amplitude but reverse polarities through the outside and inside coils). The solid and dashed traces correspond to those of the first (bottom) and fifth (top) wafers and the dotted trace corresponds to that of the third (middle) wafer

The magnetic vectors of *Figure 3*(c) appear to satisfy the requirements of a superconducting disk; B_r at the rim of the disk, an important parameter for lift, is greater than B_r in *Figure 3*(a). Because B_r due to the supercurrents in the penetration depths of the top and bottom surfaces, though nearly identical in magnitude, point in the opposite directions, their net contribution to lift and pitch stability is nearly zero. Neither do they have much effect, compared with that flowing at the rim, on lateral stability. We may thus proceed in the following analysis by neglecting the supercurrents at the top and bottom surfaces.

Field-cool (FC) and zero-field-cool (ZFC) processes

In the electromaglev experiment, a normal-state YBCO sample may be cooled to the superconducting state by either a field-cool (FC) or zero-field-cool (ZFC) process.

Field-cool (FC). The FC process follows the steps described below[3].

1. Start energizing the electromagnets, exposing a *virgin* superconducting sample resting atop the magnet system to an increasing magnetic field.
2. Hold the field at H_{fc1} when the *virgin* sample begins levitating, tilted. H_{fc1} is the z-directed field by the magnet system at the rim of the sample.
3. Remove the sample from the magnet system and warm it up to the normal state.
4. Place the sample back atop the magnet system and let it become superconducting in the presence of H_{fc2}, the z-directed field by the magnet system at the rim. H_{fc2} can be equal to, greater, or even slightly smaller than H_{fc1}. In our analysis of the disk, the z-axis induction at the rim of the top wafer at H_{fc2} is designated B_{i0}.

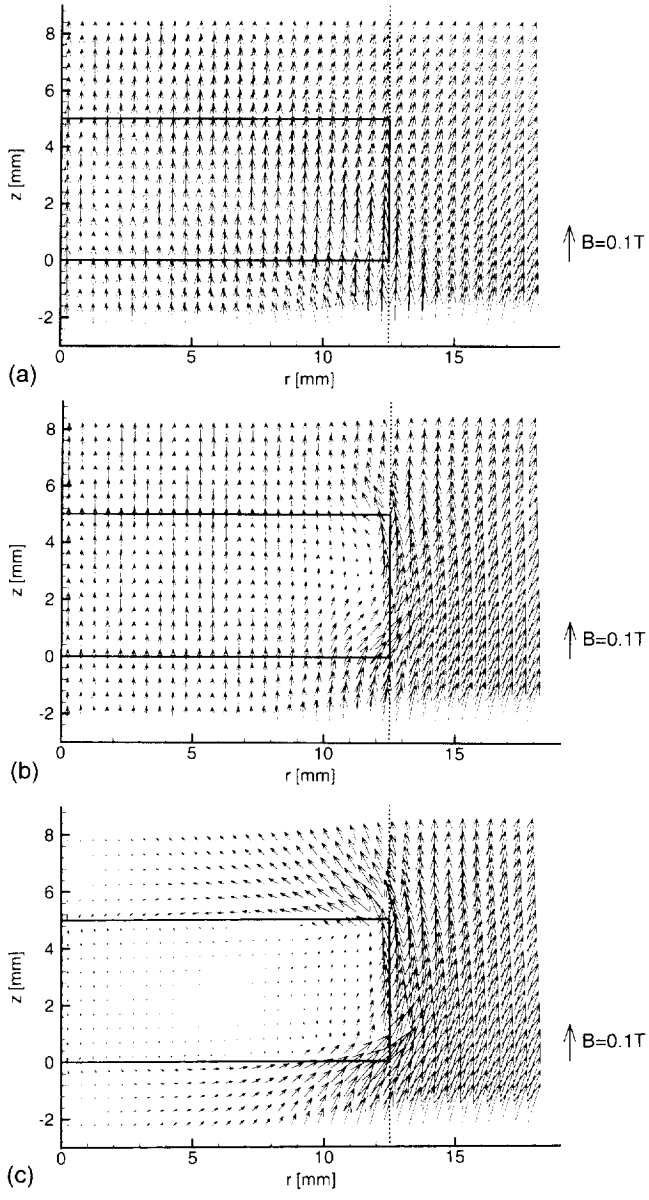

Figure 3 Three graphs of magnetic vectors, where in each graph the right-hand half of the disk is outlined as a rectangle: (a) magnetic vectors due to the magnet system alone; (b) magnetic vectors of (a) plus those due to the supercurrent flowing in the penetration depth; and (c) magnetic vectors of (b) plus those due to the supercurrents flowing in the penetration depths at both top and bottom surfaces. Also indicated in each graph is the dotted line corresponding to the boundary of a long cylinder of radius R_d

5. There are two options for the next step, steps 5(a), 5(b), and 6 or steps 5(c) and 6.
   (a) Reduce the field from H_{fc2} to zero. The trapped flux of the disk is also denoted by B_{i0}. The supercurrent generating this trapped flux in turn generates a field whose z-axis induction at the rim of the top wafer is denoted $-B_0$.
   (b) Increase the field from zero. The *nonvirgin* sample now floats stably, tilt-free, at field $H_{h'} > H_{fc2}$. Note that $H_{fc2} > H_{fc0}$, where H_{fc0} is the minimum z-axis field at the rim of the sample required to ensure tilt-free stable levitation in the FC process.
   (c) Increase the field starting at H_{fc2}; the *nonvirgin* sample levitates, tilt-free, at $H_{h'}$.
6. At $H_{z0} > H_{h'}$, the sample levitates tilt-free at height $d >$ 0, where d is measured from the center of the coils to the bottom surface of the sample. The z-axis induction at the rim of each wafer at $H_{h'}$, at which the disk just begins to levitate, is denoted B_{z0}.

Zero-field-cool (ZFC). In the ZFC process, the sample is cooled from the normal state to the superconducting state in zero field. No trapped flux is thus induced in the sample, which remains *virgin*. Tilt-free stable levitation is not possible with the virgin sample. Note that the ZFC process is a special case of the FC process in which $H_{fc2} = 0$.

Field and current density distributions. *Figure 4* presents examples of field and supercurrent density distributions within the disk along its x-axis ($-R_d \leq x \leq +R_d$) at $y = 0$ for the FC (*Figure 4*(a and b)) and ZFC (*Figure 4*(c)) processes. Both *Figure 4*(a and b) show field distributions, $B_z(x)$ after step 5(a) (the light lines, from left to right, connecting B_0, B_{i0} and B_0) and step 5(b) or 5(c) (the heavy lines, from B_{z0} at the left-hand side and B_{z0} at the right-hand side), and corresponding supercurrent distributions, J_θ, derived from the B_z distributions with J_c assumed field-independent. In *Figure 4*(a), B_{z0} is less than $2B_{i0} - B_0$ ($B_{z0} \leq 2B_{i0} - B_0$), whereas in *Figure 4*(b), B_{z0} is greater than $2B_{i0} - B_0$ ($B_{z0} > 2B_{i0} - B_0$). The significance of the difference between the two cases is evident from both B_z and J_θ distributions. When $B_{z0} \leq 2B_{i0} - B_0$ (*Figure 4*(a)), there is a thin annular region within the disk where B_z dips below B_{i0}. Within this annulus a supercurrent flows in the direction opposite to that of the supercurrent flowing at the rim; this current reversal has a great influence on stability. When $B_{z0} > 2B_{i0} - B_0$ (*Figure 4*(b)), B_z and J_θ distributions are essentially identical to those of the ZFC process (*Figure 4*(c)). It may also be noted that an asymmetry in the J_θ distribution necessarily implies the presence of J_r so as to satisfy the conservation of net current.

In this paper, the field and supercurrent density distributions within a sample are evaluated through the straight application of a numerical analysis, results of which are illustrated, for example, in *Figure 4*. For evaluation of a system like the present one in which spatial changes in field and supercurrent density distributions are small, FEM techniques[7,8] would use an enormous amount of computation time and thus is, we believe, less suitable than the numerical analysis.

Levitation height

For a superconducting disk of radius R_d and thickness δ_d, symmetric in the θ-direction with an r- and z-dependent supercurrent density, $J_\theta(r,z)$, and exposed to an r- and z-dependent magnetic induction, $B_r(r,z)$, lift, F_z, at a levitation height d is given by:

$$F_z = \int_d^{d+\delta_d} \int_0^{R_d} 2\pi J_\theta(r,z) B_r(r,z) r \, dr \, dz \qquad (4)$$

Equation (4) was solved with the disk first divided axially into five wafers, each $\delta_d/5$ thick, and then with the penetration region of the nth wafer ($R_d - \delta_{\lambda_n} \leq r \leq R_d$) divided radially into 15 rings, the mth ring having a radial

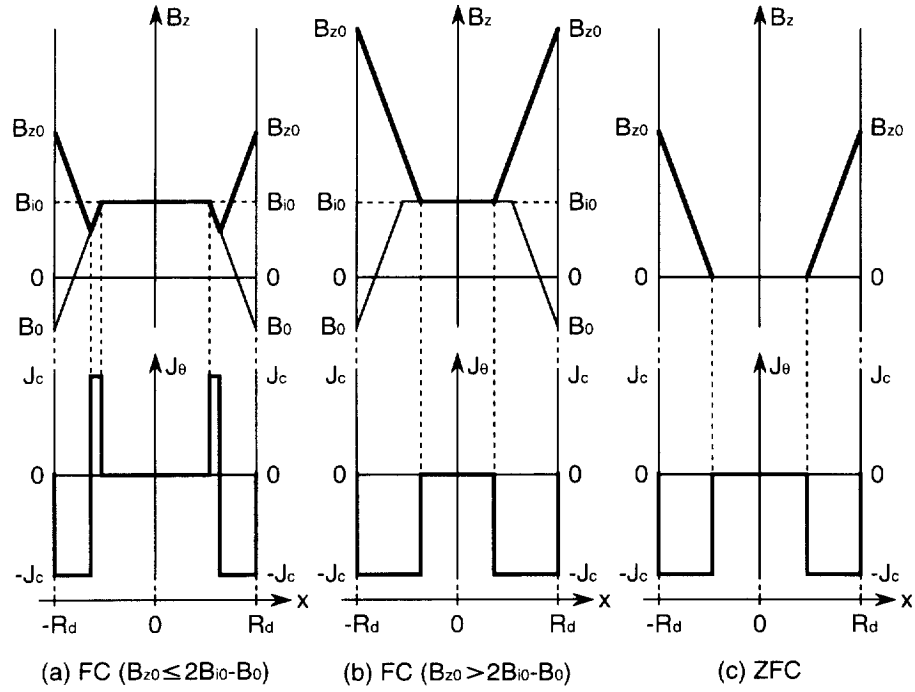

Figure 4 Examples of field and supercurrent distributions within the disk along the x-axis ($-R_d \le x \le +R_d$) at $y = 0$. (a) FC process in which $B_{z0} \le 2B_{i0} - B_0$; (b) FC process in which $B_{z0} > 2B_{i0} - B_0$; (c) ZFC process

build of $\Delta\lambda_{(m,n)}$. Within each of the 75 rings, B_r and J_θ are assumed constant. Thus, Equation (4) becomes:

$$F_z = \frac{2\pi\delta_d}{5} \sum_{m=1}^{15} \sum_{n=1}^{5} \{\Delta\lambda_{(m,n)} r_{(m,n)} J_\theta[r_{(m,n)}, z_n] B_r[r_{(m,n)}, z_n]\} \tag{5}$$

In Bean's critical-state model, J_θ in the superconductor can be 0, J_c, or $-J_c$, depending on the history of field exposure, in this case, to H_z. Thus, J_θ within each of the subdivisions of the disk is: (1) $-J_c$ for $d H_z/dr > 0$; (2) 0 for $d H_z/dr = 0$; or (3) $+J_c$ for $d H_z/dr < 0$.

At a levitation height of d, lift F_z is balanced by the weight of the disk $M_d g$, where M_d is its mass, with a modification to include the buoyancy of the liquid since the disk in this study series levitates immersed in liquid nitrogen. At height, d, the disk is in equilibrium:

$$F_z = (M_d - V_d \varrho_{LN2}) g \tag{6}$$

where V_d is the volume of the disk and ϱ_{LN2} is the density of liquid nitrogen.

Lateral stability

Lateral stability is the ability of a levitated sample to return to its original equilibrium position when displaced by a small distance in the lateral direction. In our analytical model of the disk under consideration, the disk, already divided into 75 rings, is further dissected azimuthally into 12 equal sections, as shown in *Figure* 5(a). This is to take into account the asymmetry of the magnetic field and current distributions caused by a displacement of the disk by Δx in the x-direction (*Figure* 5(b)). Then the total lateral force F_x is given by:

$$F_x = \frac{\pi\delta_d}{30} \sum_{m=1}^{15} \sum_{n=1}^{5} \sum_{p=1}^{12} \{\Delta\lambda_{(m,n,p)} r_{(m,n,p)} J_\theta[r_{(m,n,p)}, z_n, \theta_p] B_z[r_{(m,n,p)}, z_n, \theta_p] \cos\theta_p\} \tag{7}$$

where $\theta_p = \frac{\pi}{6}\left(p - \frac{1}{2}\right)$, as indicated in *Figure* 5(a), is in the x–y plane and measured from the $+x$-axis. For lateral stability, the following condition is required: $\partial F_x/\partial x < 0$.

Pitch stability

Pitch stability is the ability of a levitated sample to return to its original tilt-free orientation when it is rotated by a

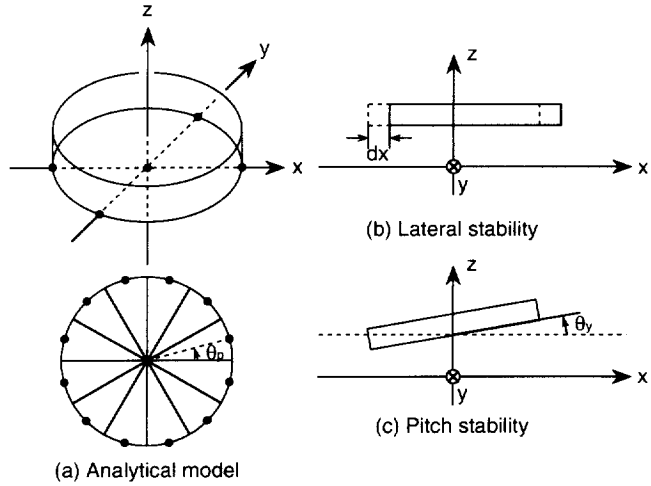

Figure 5 (a) Disk placed at the x–y–z coordinates and divided into 12 equal sections in the azimuthal direction. (b) Disk position for lateral stability analysis, showing a displacement of dx in the $+x$ direction. (c) Disk position for pitch stability analysis, showing a rotation of θ_y about the $-y$-axis

small angle about the y-axis—more generally about the r-axis. When rotated by a small angle θ_y about the y-axis, the moment, M_y, is generated by both lift F_z and lateral force F_r acting on the sample. For a small angle of rotation, the moment by the lateral force is much less than that by lift and it may be ignored. M_y due to F_z on the disk under consideration rotated by θ_y about the $-y$-axis (*Figure 5*(c)) is thus given by:

$$M_y = \frac{\pi\delta_d}{30}\sum_{m=1}^{15}\sum_{n=1}^{5}\sum_{p=1}^{12}\{\Delta\lambda_{(m,n,p)}r^2_{(m,n,p)} \times J_\theta[r_{(m,n,p)},z_n,\theta_p]B_r[r_{(m,n,p)},z_n,\theta_p]\cos\theta_p\cos^2\theta_y\} \quad (8)$$

where, again, $\theta_p = \frac{\pi}{6}\left(p - \frac{1}{2}\right)$. For pitch stability, the required condition is: $\partial M_y/\partial\theta_y < 0$.

Results and discussion

Magnetic field

In the FC process, B_{i0} (trapped field, after step 4) as well as B_0, (magnetic field at the rim with the external field zero, after step 5(a)) are the key parameters required to determine the penetration depth. B_0 is estimated iteratively as follows.

(a) Set B_0 zero initially: $B_0 = 0$.
(b) Determine a penetration depth with $B_0 = 0$ and B_{i0}.
(c) Compute B_0 using the net supercurrent in the penetration depth of step (b).
(d) Recompute the penetration depth with B_{i0} and B_0 determined in step (c).
(e) Repeat steps (c) and (d) until B_0 converges.

The above sequence was used to determine B_z in the presence of an external field generated by the magnet system. The trapped field B_{i0} is approximated to be the same as the external induction of the magnet system at a field of H_{fc2} in step 4 of the FC process.

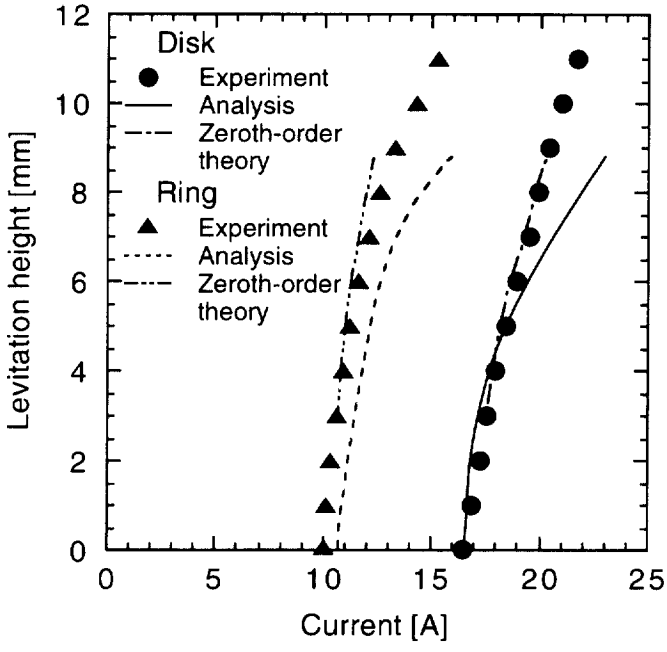

Figure 6 Two sets of levitation height d vs. magnet current I data, one for the disk and the other for the ring. Circles (disk) and triangles (ring) are experimental[3]; solid (disk) and dotted lines (ring) are analytical; and dashed (disk) and double-dashed (ring) lines are based on the zeroth-order theory[1-3]

Levitation height

Figure 6 presents two sets of levitation height d vs. I (magnet current) data, one for the disk and the other for the ring. Circles and triangles, respectively, for the disk and ring are experimental; solid (disk) and dotted lines (ring) are analytical. (Results based on the zeroth-order theory are given by the dashed and double-dashed lines, respectively,

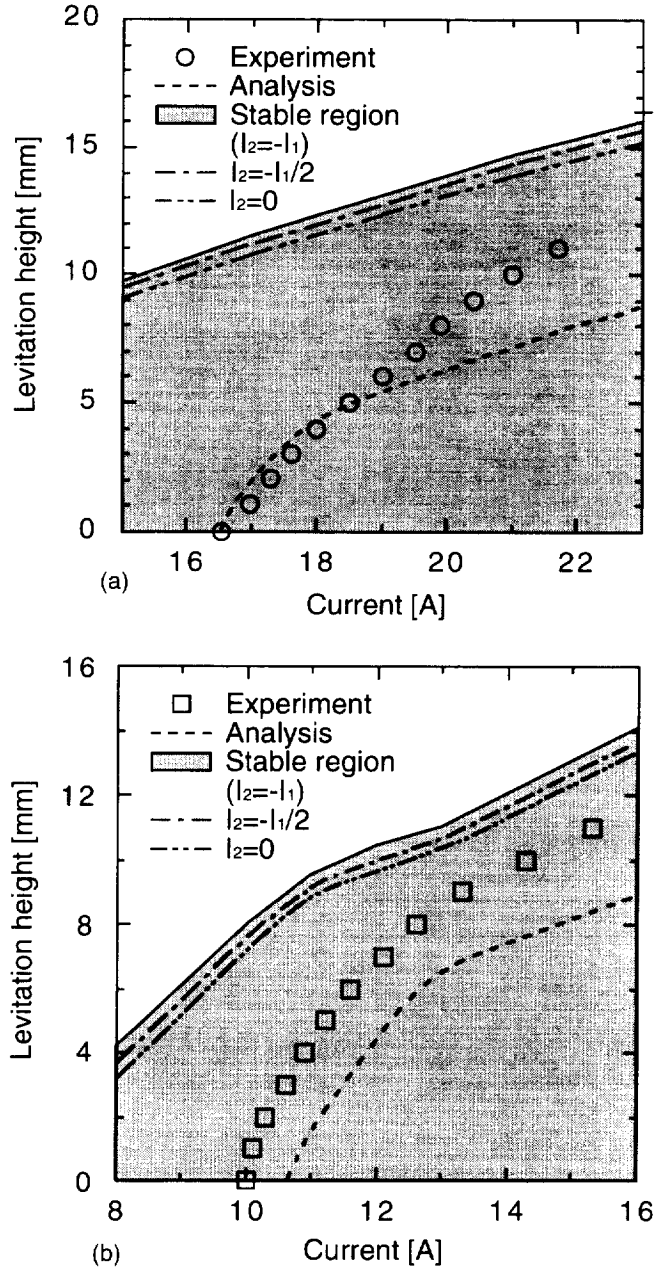

Figure 7 d vs. I diagrams indicating stable regions for three combinations of I_1 (outside coil current) and I_2 (inside coil current): (a) disk; and (b) ring. In each diagram the stable region has three outer boundaries—the solid ($I_2 = -I_1$, used in the experiment)[3], dashed ($I_2 = -0.5I_1$), and double-dashed ($I_2 = 0$). Also shown are d vs. I plots, experiment (circles for the disk and squares for the ring)[3] and present analysis (dotted lines for both disk and ring)

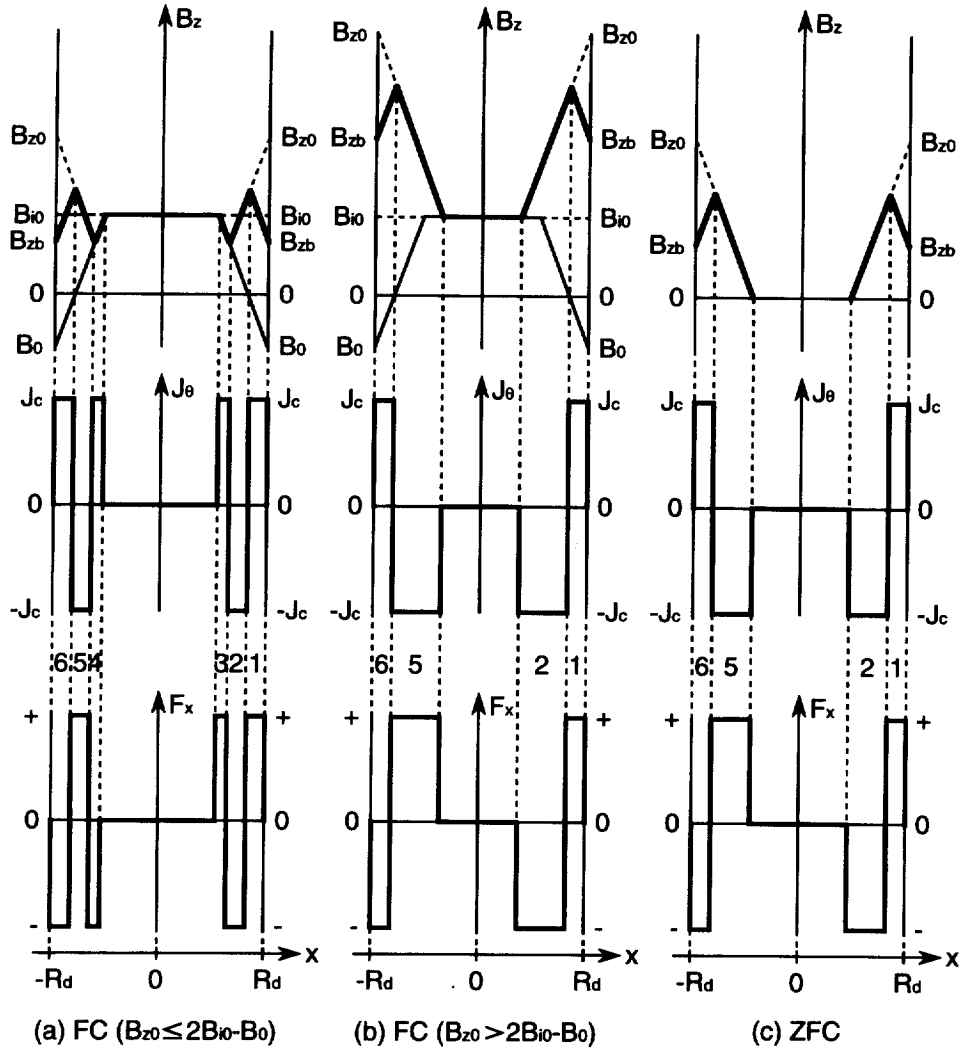

Figure 8 Three sets of schematic drawings for $B_z(x)$, $J_\theta(x)$, and $f_x(x)$ (force density in the x-direction) distributions across the disk at $y = 0$ in equilibrium: (a) FC process in which $B_{z0} \leq 2B_{i0} - B_0$; (b) FC process in which $B_{z0} > 2B_{i0} - B_0$; (c) ZFC process

for the disk and ring.) The computed lines—this analysis and zeroth-order theory—include the buoyancy effect of liquid nitrogen. Agreement between experiment and theory (this analysis) is reasonable. Note that both experimental and analytical curves show a clear-cut transition. The discrepancy is due chiefly to an overestimation in the analysis of the trapped flux, B_{i0}; agreement should be improved with a trapped flux smaller than B_{i0}.

Agreement between theory and experiment in *Figure 6* is better with the zeroth-order theory than with the present analysis. This should not lead to the conclusion that the zeroth-order theory is as good as or even better than the present analysis. As pointed out earlier, the zeroth-order theory does not take into account the presence of trapped flux in a sample nor the irreversibility of supercurrent distribution. Thus, the theory can predict quite accurately the dependence of levitation height with respect to magnet current, provided it is adjusted to a particular data point, as illustrated in *Figure 6*; it is unable to predict correct levitation height for a sample with an arbitrary value of trapped flux. Lack of trapped flux in the theory also makes it unsuitable to deal with lateral and pitch stabilities in a more general way.

The present analysis has also been applied to determine the magnet current corresponding to H_{fc0} for each sample. As described earlier in connection with the field-cool (FC) process, H_{fc0} is the minimum z-axis field at the rim of the sample required to ensure tilt-free stable levitation (step 5(b)). According to this analysis, currents to generate H_{fc0} are 8.1 A and 5.7 A, respectively, for the disk and ring; respective currents determined in the experiment are 8 A and 6 A. Agreement between theory and experiment is quite good.

Lateral and pitch stability

Figure 7 shows d vs. I graphs of stable regions for the disk (*Figure 7*(a)) and ring (*Figure 7*(b)) samples, for three sets of I_1 and I_2, currents, respectively, for outside and inside coils. In each graph, the stable region is bounded by the solid, dashed, and double-dashed lines, respectively, for sets of $I_2 = -I_1$ (experiment), $I_2 = -0.5I_1$, and $I_2 = 0$. In addition, each graph also includes d vs. I plots, experiment (circles or squares) and this analysis (dotted lines), for both samples. Agreement between experiment and analysis is fair. Results of *Figure 7* imply that stable levitation is achievable without inside coil, which is energized to generate a magnetic field directed opposite from that of outside coil and extend the 'magnetic well' ($\partial B_z/\partial r > 0$) profile over a larger axial span than otherwise possible with outside coil alone.

Figure 8 shows three sets of schematic drawings for

$B_z(x)$, $J_\theta(x)$, and $f_x(x)$ distributions across the disk at $y = 0$ with the disk at the center. $f_x(x)$ represents force density in the x-direction; here only its polarity, not amplitude, is significant. The distributions are for FC processes (*Figure 8*(a and b)) and the ZFC process (*Figure 8*(c)). In each set, the penetration region of the disk is divided into annular zones, in *Figure 8*(a), for example, into six zones, labelled 1 to 6. Because the external field is symmetric about the z-axis, so are the $B_z(x)$, $J_\theta(x)$, and $f_x(x)$ distributions in each set. However, depending on the size of B_{z0} relative to $2B_{i0} - B_0$, i.e., $B_{z0} \leq 2B_{i0} - B_0$ (as in *Figure 8*(a)) or $B_{z0} > 2B_{i0} - B_0$ (as in *Figure 8*(b)), there are subtle differences in these distributions between the two FC processes, as discussed earlier in connection with *Figure 4*.

Figure 9 shows similar sets of drawings for the disk displaced by dx in the x-direction: *Figure 9*(a) for $B_{z0} \leq 2B_{i0} - B_0$ (FC1 process) and *Figure 9*(b) for $B_{z0} > 2B_{i0} - B_0$ (FC2 process); and *Figure 9*(c) for the ZFC process. B_{za} is the flux at the rim of the disk upon displacement. (B_{zb} in *Figure 8* is the flux at the rim of the disk in equilibrium.) Because $B_z(x)$ is now asymmetric, so are $J_\theta(x)$ and $f_x(x)$. Note that in each set the displacement: (1) creates a new annular zone (labelled 0) in the right-hand side; (2) decreases zones 1 and 5; and (3) increases zone 6. (For the sake of brevity, henceforth a 'zone' refers to the size of a zone; also FC and ZFC refer, respectively, to the FC and ZFC processes.) These changes all contribute to enhance the net lateral restoring force, implying that the condition of $\partial B_z/\partial r > 0$ that causes these changes ensures lateral stability. Note that the ratio of zone 2 to zone 1 in J_θ distribution, because zone 2 current generates a restoring force and zone 1 current an unstabilizing force, is important for lateral stability. Because zone 2 of FC1 is much smaller than that of ZFC, the ratio of zone 2 to zone 1 is much smaller for FC1 than that for ZFC: for lateral stability ZFC thus provides a condition more favorable than FC1. As noted earlier that an asymmetry in the J_θ distribution necessarily implies the presence of J_r; J_r, however, has no direct impact on stability.

Figure 10 shows three sets of schematic drawings for distributions across the disk at $y = 0$ of $B_z(x)$, $J_\theta(x)$, and $m_y(x)$ (moment density about the y-axis) with the disk in equilibrium: *Figure 10*(a) for $B_{z0} \leq 2B_{i0} - B_0$ and *Figure 10*(b) for $B_{z0} > 2B_{i0} - B_0$, both FC; and *Figure 10*(c) for ZFC. Note that the m_y distribution indicates only polarities (the + sign for moment density in the + y-direction and the − sign for moment in the − y direction). As before, the penetration region of the disk for each FC is divided into six annular zones, 1 to 6. As in *Figure 8* the sets have symmetrical distributions along the x-axis. Also as in *Fig-*

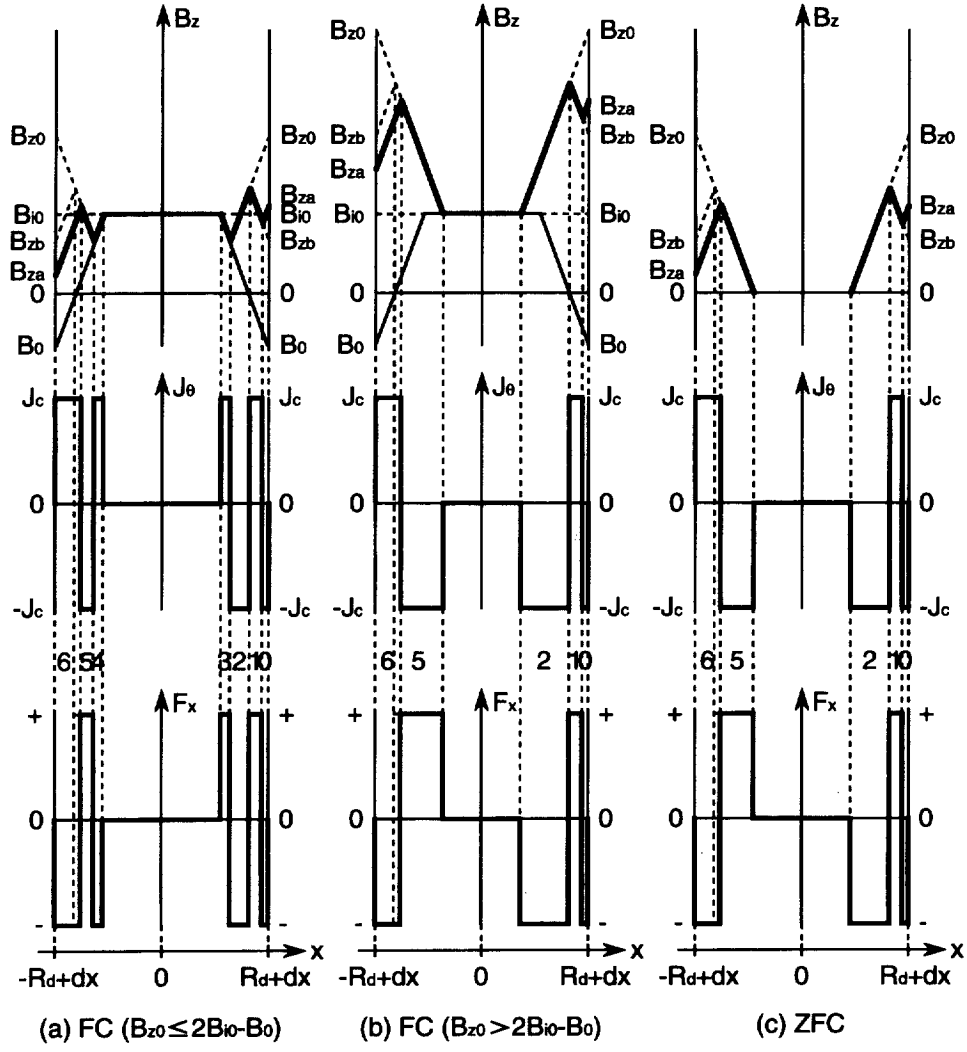

Figure 9 Three sets of drawings for $B_z(x)$, $J_\theta(x)$, and $f_x(x)$ (force density in the x-direction) distributions across the disk at $y = 0$ with the disk displaced by dx in the x-direction: (a) FC process in which $B_{z0} \leq 2B_{i0} - B_0$; (b) FC process in which $B_{z0} > 2B_{i0} - B_0$; (c) ZFC process

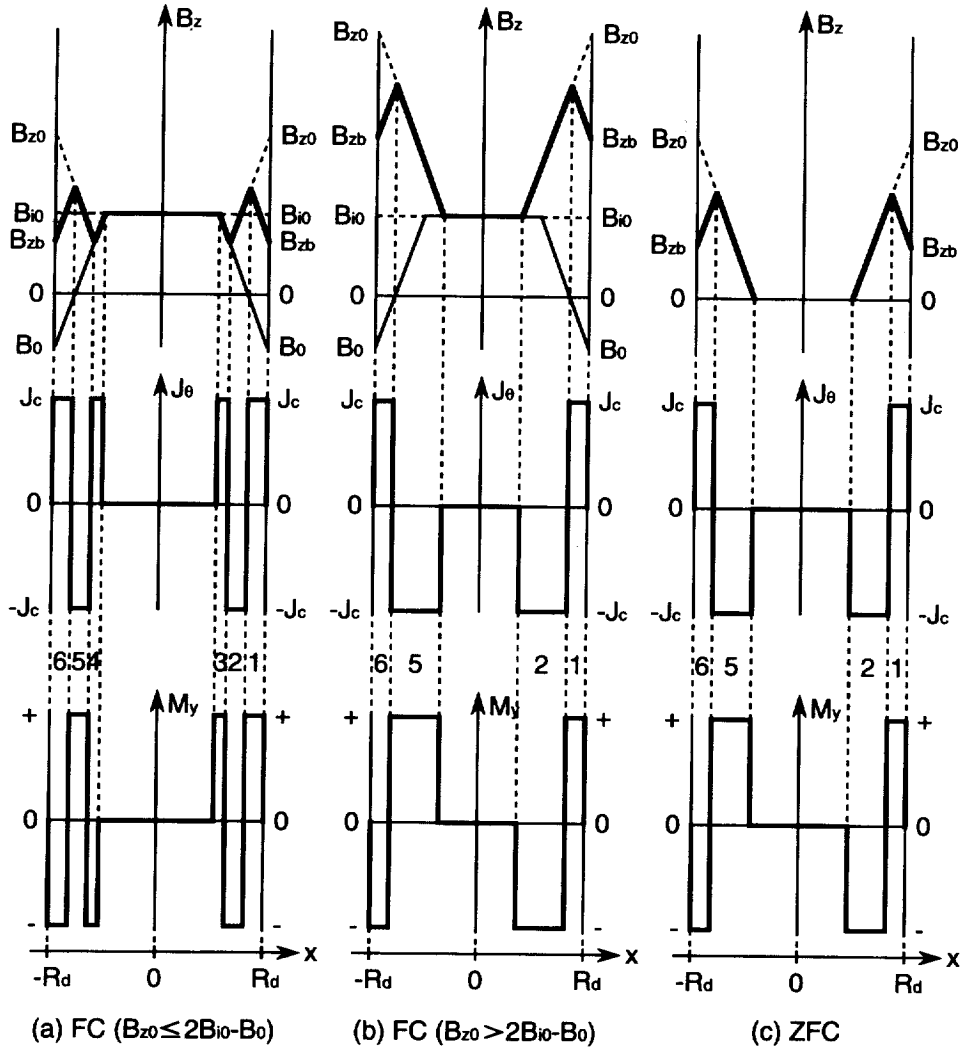

Figure 10 Three sets of schematic drawings for $B_z(x)$, $J_\theta(x)$, and $m_y(x)$ (moment density about the y-axis) distributions across the disk at $y = 0$ in equilibrium: (a) FC process in which $B_{z0} \leq 2B_{i0} - B_0$; (b) FC process in which $B_{z0} > 2B_{i0} - B_0$; (c) ZFC process

ure 8, there are subtle differences in distributions between those in *Figure 10*(a) and those in *Figure 10*(b).

Figure 11 shows similar sets of drawings with the disk rotated by angle θ_y about the $-y$-axis: *Figure 11*(a) for $B_{z0} \leq 2B_{i0} - B_0$ and *Figure 11*(b) for $B_{z0} > 2B_{i0} - B_0$, both FC processes; and *Figure 11*(c) for the ZFC process. As in *Figure 9*, because $B_z(x)$ is asymmetric, so are $J_\theta(x)$ and $m_y(x)$. Note that in each distribution the displacement: (1) creates a new annular zone (labelled 7); (2) decreases zones 2 and 6; and (3) increases zone 1. These changes, together with an increase of B_r in zone 1 and decreases of B_r in zones 4 and 6 (*Figure 11*(a)) and in zone 6 (*Figure 11*(b)), all contribute to make the disk pitch-stable. On the other hand, a combination of an increase of B_r in zone 2 and decreases of B_r in zones 5 and 7 makes the disk pitch-unstable. Trapped flux is a decisive factor in making each of these rotation-induced changes, B_r and zone size, either stabilizing or unstabilizing. Thus, when trapped flux is small, which applies also to ZFC, zone 2 becomes generally much larger than zone 1, and zone 5 is much larger than zones 6 and 7, making B_r effects dominate zone effects and hence makes the disk pitch unstable. (Note that the distributions shown in *Figures 4, 8–11* are all *schematic* and do not present relative sizes accurately; some are drawn much larger than the actual sizes for the sake of clarity.) Conversely, the greater the trapped flux, the greater the zone effects, making the disk pitch stable, provided that the trapped flux is sufficiently great. As stated earlier, a key parameter is H_{fc2}, which is the trap-flux-inducing field in step 4 of the FC process. Note that H_{fc2} must be at least H_{fc0}.

Minimum radial build

Among the four samples examined, the ring has been judged best based on the lift-to-weight criterion[3]. Here we may distinguish a ring from an annulus in terms of its radial build, $\Delta R(= R_d - R_{in})$, where R_{in} is the inside radius of the ring: we may call an annulus a ring if $\Delta R < R_d/2$ and an annulus an annulus if $\Delta R > R_d/2$. If a ring is the best, the next obvious question is 'how small can its radial build be?' As demonstrated in the experiment[1,2], a BSCCO-2223 tape solenoid is unstable, perhaps in part because, unlike the YBCO annulus and ring, it is multi-turned and most likely because the effective thickness of the superconducting layer of the tape is too thin to satisfy another requirement for stable levitation: at least two degrees of freedom for spatial supercurrent flow[1,2]. We shall thus now examine the radial build of the ring, specifically its minimum thickness to satisfy this spatial flow requirement.

Figure 12 illustrates two sets of $B_z(x)$ and $J_\theta(x)$ distributions for ring 1 (*Figure 12*(a)) and ring 2 (*Figure 12*(b)) having the same outer radius (R_d), thickness (δ_d), and the

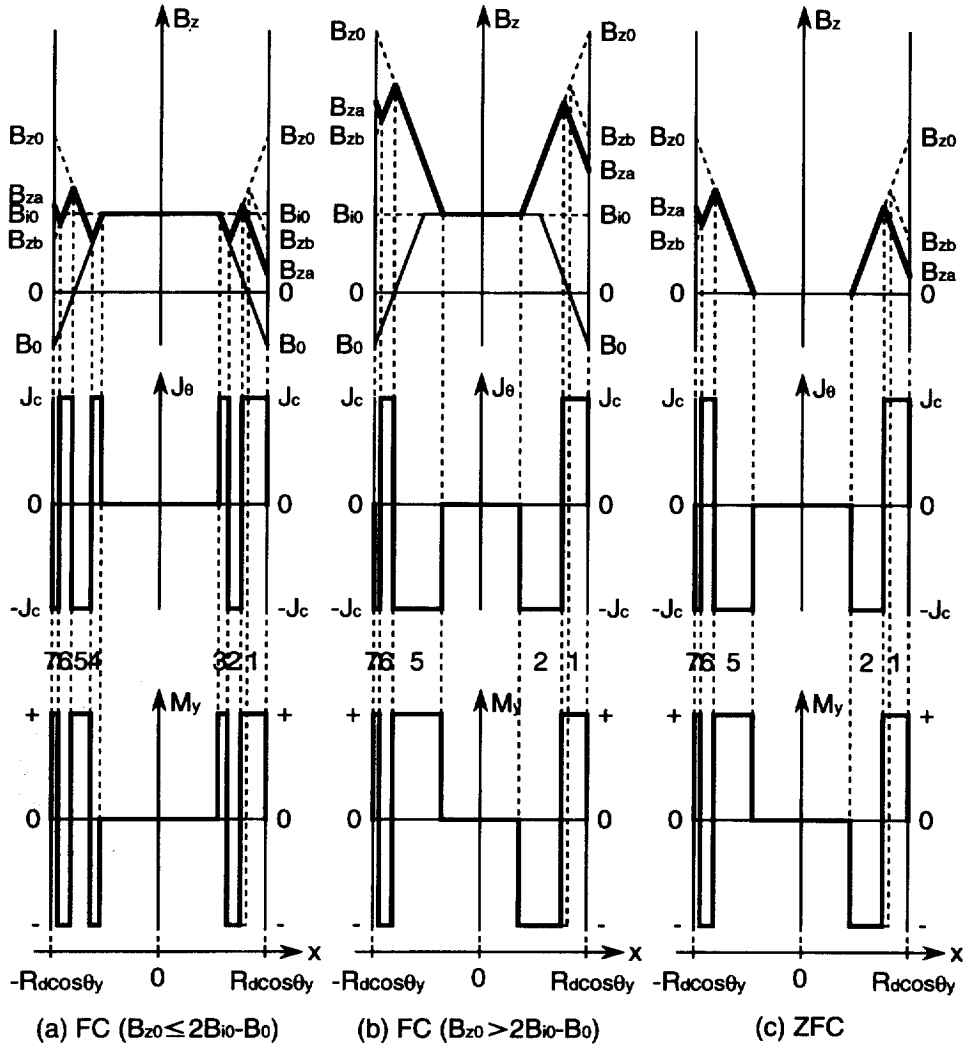

Figure 11 Three sets of schematic drawings for $B_z(x)$, $J_\theta(x)$, and $m_y(x)$ (moment density about the y-axis) distributions across the disk at $y = 0$ with the disk rotated by angle θ_y about the $-y$-axis; (a) FC process in which $B_{z0} \leq 2B_{i0} - B_0$; (b) FC process in which $B_{z0} > 2B_{i0} - B_0$; (c) ZFC process

same level of trapped flux but with different radial thicknesses, ring 1 being thicker (and thus heavier) than ring 2. To achieve a given levitation height, ring 1 thus requires an external field greater than does ring 2, making, as seen in *Figure 12*(a and b), B_{z0} for ring 1 greater than that for ring 2. This in turn results in the J_θ zone of ring 1 being greater than that of ring 2, making ring 1 pitch-unstable and ring 2 pitch-stable. The condition that determines pitch-stability (or instability) is the relative magnitude of B_{z0} in comparison with that of $B_{z0\lim}$, which is defined in the figure. Thus, stability is ensured if $B_{z0} < B_{z0\lim}$ and vice versa. This condition has an important implication: a ring, because it is lighter, is generally more pitch-stable than a disk of the same outer radius and thickness. Because the ratio of $B_{z0}/B_{z0\lim}$ depends not only on trapped field but also on the weight of the ring, the required minimum thickness for radial build to ensure pitch stability, $\Delta R_{\min}$, may be estimated from lift, F_z, and the weight of the ring, $M_r g$, where M_r is the mass of the ring.

As an illustration, *Figure 13* shows $B_z(x)$ distributions for three rings, ring 1 (*Figure 13*(a)), ring 2 (*Figure 13*(b)), and ring 3 (*Figure 13*(c)), all having the same thickness but different ΔR. Here, it is assumed that each ring has just the right amount of trapped flux to satisfy the condition $F_z = M_r g$ and thus is levitated stably at a given height. Ring 1, having the largest ΔR among the three, is thus the heaviest, and models the ring used in our experiment. It requires a large B_{z0} to begin levitation. Ring 2, having a smaller ΔR than ring 1, models a lighter ring. Ring 2 has the same amount of trapped field (B_{i0}) as ring 1, thus requiring a smaller B_{z0} than ring 1, which, in turn, gives rise to, as evident from *Figure 13*(a and b), a $B_z(x)$ distribution that is subtly different from that of ring 1. The inside wall area of ring 2 now carries a supercurrent that flows in the direction opposite to the main supercurrent, resulting in a net reduction in lift. We may eliminate this negative supercurrent by reducing the trapped flux. Ring 3 models such a ring: its radial build is equal to a minimum level required for stable levitation, $\Delta R_{\min}$. For ring 3 with an outer diameter of 25 mm and thickness of 5 mm, $\Delta R_{\min}$ becomes ~ 50 μm, comparable with the thickness of BSCCO-2223 layers in *mono-tape* silver-sheathed tapes. The BSCCO-2223 solenoid that proved unstable in our study was wound with *multi-tape* BSCCO-2223 tape having the BSCCO-2223 layers each estimated to be one order of magnitude smaller than 50 μm. To achieve stable levitation with a one-turn ring wound of such a tape, the superconductor layer of the tape must be ~ 100 μm and thicker.

Bean's critical-state model may also be used to estimate $\Delta R_{\min}$. Here, we may assume both a supercurrent density

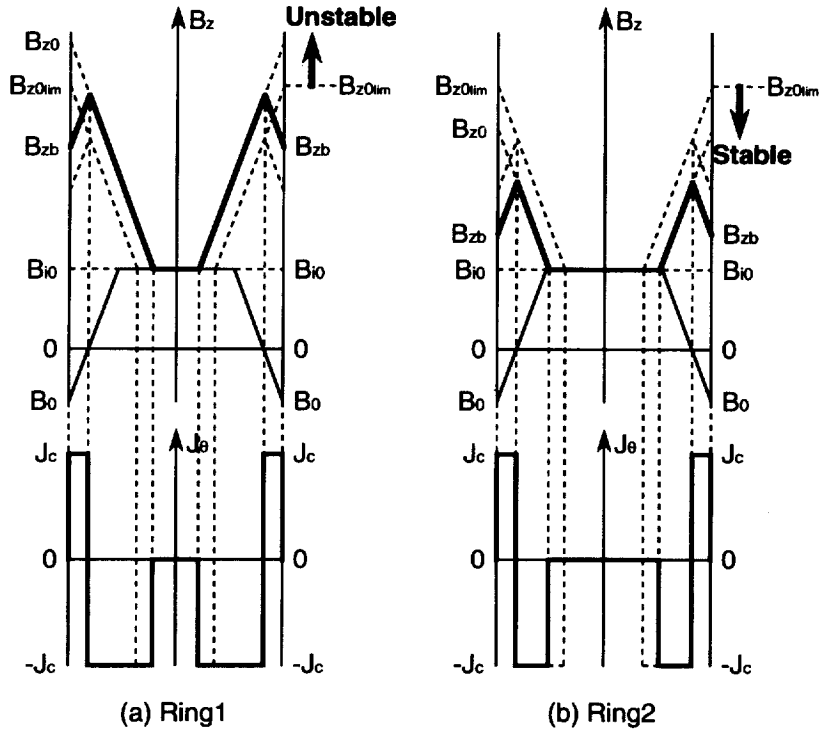

Figure 12 Two sets of $B_z(x)$ and $J_\theta(x)$ distributions for two rings of the same outer diameter but with different radial thicknesses. (a) Ring 1; (b) ring 2. Ring 1 is thicker (and thus heavier) than ring 2

of J_c and the radial component of initial magnetic flux density within the superconductor, B_{r0}, to be constant. An expression for lift, F_z, for a ring with outside radius of R_d and inside radius of R_{in} may be given by:

$$F_z = \pi(R_d^2 - R_{in}^2)\delta_d B_{r0} J_c \tag{9}$$

Because our levitation experiments[1-3] have all been performed with each YBCO sample immersed fully in a bath of liquid nitrogen boiling at 77 K, the buoyancy effect of the liquid nitrogen must be included. The effective weight of the ring, $[M_r\, g]_{\text{eff}}$, is thus given by:

$$[M_r g]_{\text{eff}} = \pi(R_d^2 - R_{in}^2)\delta_d(\varrho_d - \varrho_{LN2})g \tag{10}$$

where ϱ_d and ϱ_{LN2} are densities, respectively, of the material of the ring (6400 kg/m^3 for YBCO) and liquid nitrogen (807 kg/m^3). From the equilibrium condition, $F_z = [M_r\, g]_{\text{eff}}$, we obtain an expression for B_{r0}:

$$B_{r0} = \frac{(\varrho_d - \varrho_{LN2})g}{J_c} \tag{11}$$

Both magnetic flux densities, B_{r0} and B_{z0}, are proportional to the magnet current. Therefore we may express B_{r0} in terms of B_{z0}:

$$B_{r0} = CB_{z0} \tag{12}$$

where C is a proportionality constant. From the $B_z(x)$ diagram of ring 3, shown in *Figure 13*(c), trapped field B_{i0} is clearly one half of B_{z0}, i.e., $B_{i0} = B_{z0}/2$. The penetration depth of the supercurrent for this ring (*Figure 13*(c)), λ_R, is equal to $R_d - R_{in}$, which is, by definition, equal to $\Delta R_{\min}$ here.

$$\lambda_R = R_d - R_{\min} \equiv \Delta R_{\min} \tag{13}$$

Using Bean's critical-state model, we have:

$$\Delta R_{\min} = \frac{B_{i0}}{\mu_o J_c} \tag{14}$$

Combining Equations (11)–(14), we have an expression for $\Delta R_{\min}$:

$$\Delta R_{\min} = \frac{(\varrho_d - \varrho_{LN2})g}{2C\mu_o J_c^2} \tag{15}$$

In our system, C is 0.099 and inserting appropriate values for parameters of Equation (15), e.g., $J_c = 10^8$ A/m^2, we obtain: $\Delta R_{\min} = 20$ μm, which is of the same order as ~ 50 μm computed in the numerical analysis. This discrepancy of ~ 30 μm comes about because here $\Delta R_{\min}$ is derived without meeting the condition that trapped flux must be of a sufficient level for pitch stability. Note that $\Delta R_{\min}$ depends inversely on J_c^2.

Conclusions

Field solutions have been obtained numerically to compute levitation height and define stability criteria for a superconducting disk sample in an 'electromaglev' ('active-maglev') system. Our analysis assumes that the disk, which otherwise obeys the Bean critical-state model, traps flux when cooled in the presence of a field from the normal state to the superconducting state. The analysis confirms a key experimental finding that the trapped flux is another essential element for determining levitation height and ensuring tilt-free stable levitation. For stability, trapped flux is in addition to at least two degrees of freedom for spatial supercurrent flow and the profile conditions imposed on the field generated by the magnet system. Agreement between

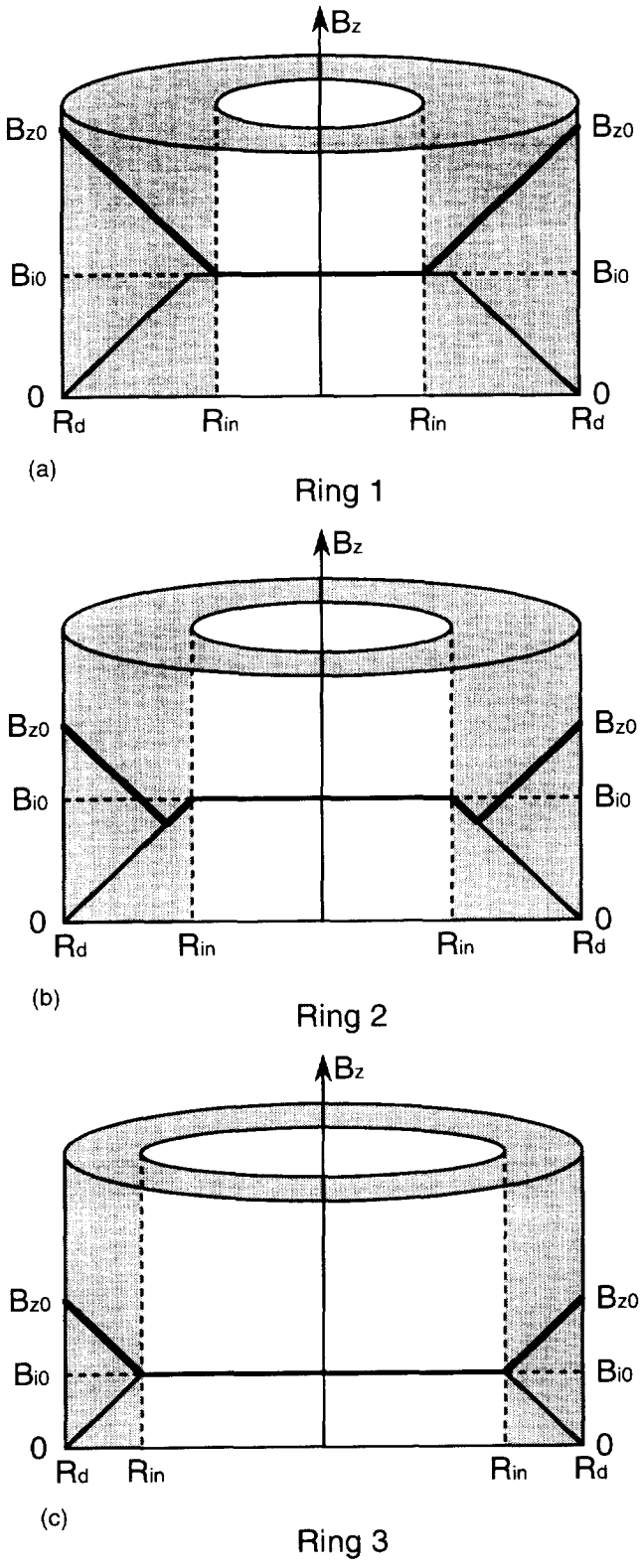

Figure 13 $B_z(x)$ distributions for three rings having the same thickness but different values of ΔR: (a) ring 1; (b) ring 2; and (c) ring 3

experiment and analysis on the dependence of levitation height on magnet current is quite good. The analysis also shows that to achieve stable levitation, a YBCO ring sample requires a radial build that is sufficiently thick to permit the supercurrent to flow in the radial direction. The minimum radial build required, ΔR_{min}, for a YBCO ring of outside radius 12.5 mm operating at 77 K is typically ~ 50 μm. An analytical expression that gives approximate values of ΔR_{min} has also been derived; ΔR_{min} depends inversely on the square of the critical current density of the superconductor.

Acknowledgement

The authors would like to express their thanks to Professor Atsushi Ishiyama for the use of Waseda University's computer facilities. Y.I. also thanks the Tokyo Electric Power Company for the opportunity to spend two 6-months periods, in 1996 and 1997, at Keio University; Professor Koichiro Sawa, his graduate students Messrs Hiroshi Horiuchi and Kentaro Nishi, and Dr Masato Murakami and Mr Ken Nagashima of ISTEC for valuable discussion and sharing their preliminary data generated at ISTEC. This work was supported in part by the US Department of Energy, Office of Basic Sciences and in part by Daikin Industries MEC Laboratory, Tsukuba, Japan.

References

1. Iwasa, Y. and Lee, H., 'Electromaglev'—magnetic levitation of a superconducting disk with a DC field generated by electromagnets: Part 1. Theoretical and experimental results on operating modes, lift-to-weight ratio, and suspension stiffness. *Cryogenics*, 1997, **37**, 807.
2. Iwasa, Y., Lee, H., Sawa, K. and Murakami, M., Active magnetic levitation with YBCO samples. In *Advances in Superconductivity IX. Proceedings of 9th International Symposium. Superconductivity (ISS'96) 21–24 October*, ed. S. Nakajima and M. Murakami. Sapporo, Springer–Verlag, Tokyo, 1997, pp. 1379.
3. Lee, H., Tsuda, M. and Iwasa, Y., 'Electromaglev' ('active-maglev')—magnetic levitation of a superconducting disk with a DC field generated by electromagnets: Part 2. Theoretical and experimental results on lift-to-weight ratio and lateral stiffness. *Cryogenics*, 1998, **38**, 419.
4. Sato, T. and Inui, Y., Three dimensional static magnetic field calculation by equivalent current of magnetization vector and its applications (in Japanese). *Denki Gakkai*, 1980, **55**(B21), 177.
5. Noguchi, S. and Ishiyama, A., Optimal design method for MRI superconducting magnets with ferromagnetic shield. *IEEE Trans. Magnet.*, 1997, **33**(2), 1904.
6. Cheng, D.K., *Field and Wave Electromagnetics* (2nd edn). Addison–Wesley Publishing Co., Reading, MA, 1990, pp. 225.
7. Hashizume, H., Sugiura, T., Miya, K., Ando, Y., Akita, A., Torii, S., Kubota, Y. and Ogasawara, T., Numerical analysis of AC losses in superconductors. *Cryogenics*, 1991, **31**, 601.
8. Mitsuru, U., Yoshida, Y., Takeda, N. and Miya, K., Experimental and numerical analysis of three-dimensional high-Tc superconducting levitation systems. *Int. J. Appl. Electromagnet. Mater.*, 1993, **4**, 13.
9. Murakami, M., *Melt Processed High-temperature Superconductors*. World Scientific Publishing Co., Singapore, 1993, pp. 101.
10. Namba, T., Kaiho, K., Ohara, T. and Koyama, K., Program for calculation of the magnetic field of an air-core cylindrical and multi-layer magnet by computer (in Japanese). *Bull. Electrotech. Lab. (Tsukuba, Japan)*, 1977, **41**, 179.

Appendix A

Equivalent current method

The magnetization vector **M** is derived as follows.

To obtain a formula for the magnetic flux density in the presence of steel plates, we let $\mathbf{m}_k$ be the magnetic dipole moment of an atom. If there are n atoms per unit volume, we define a magnetization vector, **M** [A/m], as:

$$\mathbf{M} = \lim_{\Delta V \to 0} \frac{\sum_{k=1}^{n\Delta V} \mathbf{m}_k}{\Delta V} \qquad \text{(A1)}$$

which is the volume density of magnetic dipole moment. The magnetic dipole moment $d\mathbf{m}$ of an elemental volume dV is $d\mathbf{m} = \mathbf{M}dV$ that produces a vector magnetic potential:

$$d\mathbf{A} = \frac{\mu_0 \mathbf{M} \times \mathbf{r}}{4\pi r^2} dV \tag{A2}$$

Thus:

$$\mathbf{A} = \int_V d\mathbf{A} = \frac{\mu_0}{4\pi} \int_V \mathbf{M} \times \nabla\left(\frac{1}{r}\right) dV \tag{A3}$$

where V is the volume of the magnetized steel plates. We now use the vector identity to write:

$$\mathbf{M} \times \nabla\left(\frac{1}{r}\right) = \frac{1}{r} \nabla \times \mathbf{M} - \nabla \times \left(\frac{\mathbf{M}}{r}\right) \tag{A4}$$

and expand the right-hand side of Equation A(3) into two terms:

$$\mathbf{A} = \frac{\mu_0}{4\pi} \int_V \frac{\nabla \times \mathbf{M}}{r} dV - \frac{\mu_0}{4\pi} \int_V \nabla \times \left(\frac{\mathbf{M}}{r}\right) dV \tag{A5}$$

Using a vector identity, we can change the volume integral of the curl of a vector into a surface integral. We thus have, from Equation A(5):

$$\mathbf{A} = \frac{\mu_0}{4\pi} \int_V \frac{\nabla \times \mathbf{M}}{r} dV + \frac{\mu_0}{4\pi} \int_S \frac{\mathbf{M} \times \mathbf{a}_n}{r} dS \tag{A6}$$

where $\mathbf{a}_n$ is the unit outward normal vector from dS and S is the surface enclosing the volume V. The vector magnetic potential is also expressed in terms of current density $\mathbf{J}$:

$$\mathbf{A} = \frac{\mu_0}{4\pi} \int_V \frac{\mathbf{J}}{r} dV \tag{A7}$$

A comparison of the expressions on the right-hand side of Equation A(6) with the forms of $\mathbf{A}$ in Equation A(7) suggests that the effect of the magnetization vector is equivalent to both current density $\mathbf{J}$ and surface current density $\mathbf{K}$:

$$\mathbf{J} = \nabla \times \mathbf{M} \tag{A8}$$

$$\mathbf{K} = \mathbf{M} \times \mathbf{a}_n \tag{A9}$$

Using the magnetic flux density $\mathbf{B}$ and the magnetization vector $\mathbf{M}$, we obtain:

$$\mathbf{M} = \left(\frac{1}{\mu_0} - \frac{1}{\mu}\right) \mathbf{B} \tag{A10}$$

where μ is the absolute permeability. The vector magnetic potential given by the magnetization vector can be written as:

$$\mathbf{A} = \frac{\mu_0}{4\pi} \int_V \frac{\mathbf{M} \times \mathbf{r}}{r^3} dV \tag{A11}$$

After substituting Equation A(11) into $\mathbf{B} = \nabla \times \mathbf{A}$, we obtain an expression for $\mathbf{B}$:

$$\mathbf{B} = \mathbf{B}_c + \frac{\mu_0}{4\pi} \int_V \nabla \times \left(\frac{\mathbf{M} \times \mathbf{r}}{r^3}\right) dV \tag{A12}$$

where $\mathbf{B}_c$ is the magnetic flux density generated by the electromagnets placed underneath the sample. Combining Equation A(10) and Equation A(12), we have a final governing equation:

$$\mathbf{M} - \left(\frac{1}{\mu_0} - \frac{1}{\mu}\right) \frac{\mu_0}{4\pi} \int_V \nabla \times \left(\frac{\mathbf{M} \times \mathbf{r}}{r^3}\right) dV = \left(\frac{1}{\mu_0} - \frac{1}{\mu}\right) \mathbf{B}_c \tag{A13}$$

The following approximations were used in solving Equation A(13): (1) the steel plates are divided into infinitesimal annular ring elements; and (2) the magnetization vector $\mathbf{M}$ is constant within each element. The approximations make the term that includes the magnetization volume current density zero. These approximations introduce little error to Equation A(13). The magnetic flux density $\mathbf{B}_c$ is calculated numerically by using Biot–Savart's law over the volume of conductor in the electromagnets.

Appendix B

Current vector potential method (FEM)

The governing equation in two dimensions assumes the current distribution in the axial direction to be zero and is derived as follows.

The current vector potential $\mathbf{T}$ is defined by:

$$\nabla \times \mathbf{T} = \mathbf{J} \tag{B1}$$

$$\nabla \cdot \mathbf{T} = 0 \text{(Coulomb gage)} \tag{B2}$$

$$\mathbf{n} \times \mathbf{T} = 0 \text{ (on the surface)} \tag{B3}$$

where $\mathbf{n}$ is the unit vector on the surface. Using Helmholtz's formula, the governing equation is derived as follows:

$$\nabla \times \frac{1}{\sigma_s} \nabla \times \mathbf{T} + \mu_0 \frac{\partial \mathbf{T}}{\partial t} + \frac{\mu_0}{4\pi} \int_S \frac{\partial T_n}{\partial t} \nabla\left(\frac{1}{r}\right) dS = -\frac{\partial \mathbf{B}_0}{\partial t} \tag{B4}$$

where T_n, r, and B_0 are the normal component of $\mathbf{T}$, the distance between surface and field point, and the applied flux density by the magnet system, respectively. The governing equation in two dimensions, with an assumption that the current distribution in the axial direction is zero, may be rewritten from Equation B(4) as:

$$\mathbf{n} \cdot \nabla \times \frac{1}{\sigma_s} \nabla \times (T_n \mathbf{n}) + \mu_0 \frac{\partial T_n}{\partial t} \tag{B5}$$

$$+\frac{\mu_0}{4\pi}\mathbf{n}\cdot\int_S \frac{\partial T_m}{\partial t}\nabla\left(\frac{1}{r}\right)dS = -\mathbf{n}\cdot\frac{\partial \mathbf{B}_0}{\partial t}$$

Note that Equation B(5) is identical to Equation (1) in the main text.